

Accurate Magnitude and Stress Drop using the Empirical Green's Function Method Applied to Distributed Acoustic Sensing

Itzhak Lior¹

¹Institute of Earth Sciences, The Hebrew University, Jerusalem, Israel.

Corresponding author: Itzhak Lior (itzhak.lior@mail.huji.ac.il)

Key Points:

- The Empirical Green's Function (EGF) approach was applied to 7 repeating DAS recorded earthquakes in Israel
- Accurate relative magnitudes and stress drops were calculated and stress drop was found to increase with seismic moment
- The results demonstrate the great potential of DAS for earthquake source studies

Abstract

The reliable estimation of earthquake magnitude and stress drop are key in seismology. The novel technology of distributed acoustic sensing (DAS) holds great promise for source parameter inversion owing to the measurements' high spatial density. In this study, I demonstrate the robustness of DAS for magnitude and stress drop estimation using the empirical Green's function deconvolution method. This method is applied to 7 colocated earthquakes recorded in Israel following the 2023 Turkey earthquakes. Spectral ratios were calculated using amplitude spectra stacked along the fiber, and fitted with a relative Boatwright source spectral model. Excellent fits were obtained even for similar sized earthquakes. Stable seismic moments and stress drops were calculated assuming the moment of one earthquake is known. These robust source parameters suggest that stress drop increases with seismic moment. The results demonstrate the great potential of DAS for source studies.

Plain Language Summary

Estimating earthquake magnitude and stress drop, the two most fundamental source parameters, is key for various seismological investigations, including earthquake self-similarity and hazard mitigation. The extraction of source parameters requires that source and path effects are reliably deconvolved from source contributions. One approach is to deconvolve a small earthquake from a colocated larger one in the frequency domain such that common path and site functions cancel and relative source function, between both earthquakes, remain. In this study, I apply the deconvolution approach to 7 earthquakes that followed the 2023 Turkey earthquakes, recorded using distributed acoustic sensing (DAS) applied to an optical fiber in Israel. DAS converts standard optical fibers into dense arrays, with seismic measurements every few meters along tens-of-kilometers long fibers. The deconvolution was calculated for different earthquake pairs and excellent fits were obtained with a relative source spectral model. Stable seismic moments and stress drops were calculated and their analysis suggests that stress drop increases with seismic moment. The results demonstrate the great potential of DAS for source studies.

1 Introduction

Estimating earthquake magnitudes and stress drops is fundamental for seismological research. Stress drop is key in studying earthquake self-similarity (e.g., Ide & Beroza, 2001) and strongly affects ground shaking intensity (e.g., Lior & Ziv, 2018). The estimation of these source parameters is model based, and is achieved using earthquake observations by isolating source contributions from path and site effects. Once the source term is extracted, it is fitted with a source model either in time (Al-Ismael et al., 2023; Lior & Ziv, 2018) or frequency (e.g., Huang et al., 2017; Lior & Ziv, 2017; Shearer et al., 2019) domains. The most commonly used model is the Omega-squared (Boatwright, 1980; Brune, 1970; Madariaga, 1976; Sato & Hirasawa, 1973), describing the far-field body-wave (P- or S-wave) radiation. For ground displacement it reads as:

$$\Omega(f) = \frac{\Omega_0 U_{\phi\theta}}{\left[1 + \left(\frac{f}{f_0}\right)^{2\gamma}\right]^{1/\gamma}}, \quad (1)$$

where γ equals 1 (Brune, 1970) or 2 (Boatwright, 1980), f_0 is the source corner frequency, Ω_0 is the low frequency displacement spectral plateau, and $U_{\phi\theta}$ is the radiation pattern. The latter is a function of the focal mechanism, azimuth and take-off angle from the source (Aki & Richards, 2002; Kaneko & Shearer, 2015). Ω_0 is proportional to the seismic moment M_0 divided by the

hypocentral location R ($\Omega_0 \propto M_0/R$), and to parameters that describe the media (free surface amplification factor and density and velocity at the source). Stress drop is commonly estimated assuming a simple circular crack with uniform rupture velocity (Eshelby, 1957):

$$\Delta\tau = \frac{7}{16} M_0 \left(\frac{f_0}{kC_s} \right)^3, \quad (2)$$

where C_s is the shear-wave velocity and k is a phase dependent (P or S) model constant. Equations (1) and (2) describe a simple source model with a smooth, isotropic slip distribution on a single circular patch.

Station-specific corner frequency and stress drop estimates exhibit large variability for the same earthquake for various reasons (e.g., Abercrombie et al., 2017; Kaneko & Shearer, 2015; Lior & Ziv, 2018). These variabilities are mainly attributed to the improper extraction of source from path and site contributions, a hindrance that aggravates in the presence of low signal to noise ratio (SNR) conditions, i.e., for small earthquakes. In addition, since stress drops are the cube of corner frequencies (Equations 2), small errors in f_0 translate to larger errors in $\Delta\tau$.

A common method for the reliable extraction of source contributions from path and site effects, is the empirical Green's function (EGF), or spectral ratios, method. This method uses two collocated earthquakes recorded at the same location to deconvolve the smaller earthquake (the empirical Green's function) from the larger one to remove common path, site and instrumental effects. The deconvolved spectra is then fitted with a relative source model to estimate the seismic moment ratio between both earthquakes, and the corner frequencies of each earthquake (e.g., Abercrombie et al., 2017). This approach circumvents the modeling of path and site effects, overcoming the main difficulty in estimating source parameters.

However, the EGF method suffers from several drawbacks that reduce its performance and applicability. First, the magnitudes of both earthquakes need to be sufficiently different in order to reliably fit both corner frequencies. Typically, a magnitude difference of at least 1 unit is required (e.g., Abercrombie et al., 2017; Shearer et al., 2019). Second, while path and site effects are assumed to be identical for both earthquakes, it is not necessarily the case for noise, and spectral ratios need to be stacked to suppress random noise sources and facilitate reliable model fitting (e.g., Wu et al., 2019). Third, EGF analysis is only feasible in a limited frequency band where the spectral amplitudes of both earthquakes are above a predefined noise threshold, typically set to be 3 (e.g., Viegas et al., 2010). Using a too small frequency range may bias the fitted source parameters (Abercrombie, 2021). The combined requirement of magnitude difference and SNR thresholds coupled with the need to stack multiple spectral ratios limits the applicability of the EGF method.

It has recently been demonstrated that the dense measurements of Distributed Acoustic Sensing (DAS) can be used to obtain spectral ratios (Chen, 2023). The use of DAS for source parameter estimation via the EGF method can overcome the previously described limitations of seismometer/accelerometer-based method. The application of the EGF method to DAS data is described in Text S1, with the conclusion that DAS strain (rate) data can be directly used to obtain spectral ratios (Equation S3):

$$\frac{\dot{\varepsilon}_{1j}^e(f, x)}{\dot{\varepsilon}_{2j}^e(f, x)} = \frac{M_{01} \left[1 + \left(\frac{f}{f_{02}} \right)^{2\gamma} \right]^{1/\gamma}}{M_{02} \left[1 + \left(\frac{f}{f_{01}} \right)^{2\gamma} \right]^{1/\gamma}}. \quad (3)$$

In this equation, $\dot{\epsilon}_{ij}^e(f, x)$ are strain rates of earthquake i ($i = 1, 2$) recorded at DAS channel j , and M_{0i} and f_{0i} are earthquake specific seismic moments and corner frequencies, respectively.

In this work, I demonstrate that high fidelity relative seismic moments, corner frequencies and stress drops can be obtained using DAS via the EGF method. For each earthquake, the entire fiber was reduced to a single spectrum by stacking move-out corrected Fourier spectra along the full fiber length. These earthquake specific spectra were used to obtain spectral ratios that were analyzed in the framework of Equation (3).

This manuscript is organized as follows. First, I describe the DAS data and processing. Then, I demonstrate the method using 7 well-recorded co-located earthquakes that occurred in central Israel following the devastating 2023 Kahramanmaraş Mw7.8 and Mw7.6 Eastern Turkey earthquakes. Finally, I discuss implications for earthquake self-similarity.

2 Data and Preprocessing

Following the catastrophic 2023 Kahramanmaraş Mw7.8 and Mw7.6 earthquakes in Eastern Turkey, Israel experienced a rapid increase in seismicity, including several earthquake clusters that occurred off the main Dead-Sea-Transform fault. Here, I focus on one of these clusters of co-located repeating earthquakes that were recorded by a nearby optical fiber between February 7th and 18th. Earthquakes, fiber and seismometer location are shown in Figure 1a. During this period, 10 earthquakes magnitudes 2.5 to 3.4 were recorded and cataloged by the Geological Survey of Israel. Earthquake information is listed in Table S1.

DAS earthquake data were acquired using a Prisma Photonics interrogator unit. The system is harnessing an innovative Hyper-Scan technology to produce high-quality quantitative longitudinal strain-rate measurement. Measurements were made using a 34 km long fiber installed in central Israel (Figure 1a) with a gauge length of 18.2 m, spatial sampling of 9.1 m and sampling rate of 1500 Hz. Data were then resampled to 100 Hz. Additional seismometer data from the Israeli seismic network (Kurzon et al., 2020) were used (Figure 1a).

In order to verify that the earthquakes qualify as EGF pairs, cross correlations (CC) were calculated using the nearest seismic station. Because DAS data were acquired using a horizontal fiber, with reduced P-wave sensitivity (e.g., Papp et al., 2017), the analysis focused only on S-waves. Horizontal acceleration time-series were low pass filtered at 5 Hz and CC were calculated in a 1 second window starting at the direct S-wave arrival at MEFR station (Figure 1a), located 10 km from the epicenter of the largest earthquake. Filtered time-series and CC values with respect to the largest earthquake are shown in Figure 1b. All CC values for both horizontal components were above 0.8, indicating significant similarity between the different earthquakes. Thus, it is safe to assume that these repeating earthquakes are nearly co-located and have a similar mechanism. In subsequent analysis, the catalog location of the largest earthquake (Mw3.4, Table S1) is used for all events.

Waveform similarity is also evident in the DAS recordings shown in Figure 1c, where the first 3 seconds of the S-wave are shown on a 2.2 km fiber segment. DAS CC were not calculated because of the longer epicentral distance (~ 40 km) and because single channel DAS recordings are typically characterized by lower SNR and less coherent wavefield compared to seismometers (Lior, Sladen, Rivet, et al., 2021; van den Ende & Ampuero, 2021). Similar features can be observed between the different earthquakes, for example, the coherent arrivals at the first kilometer and first half a second.

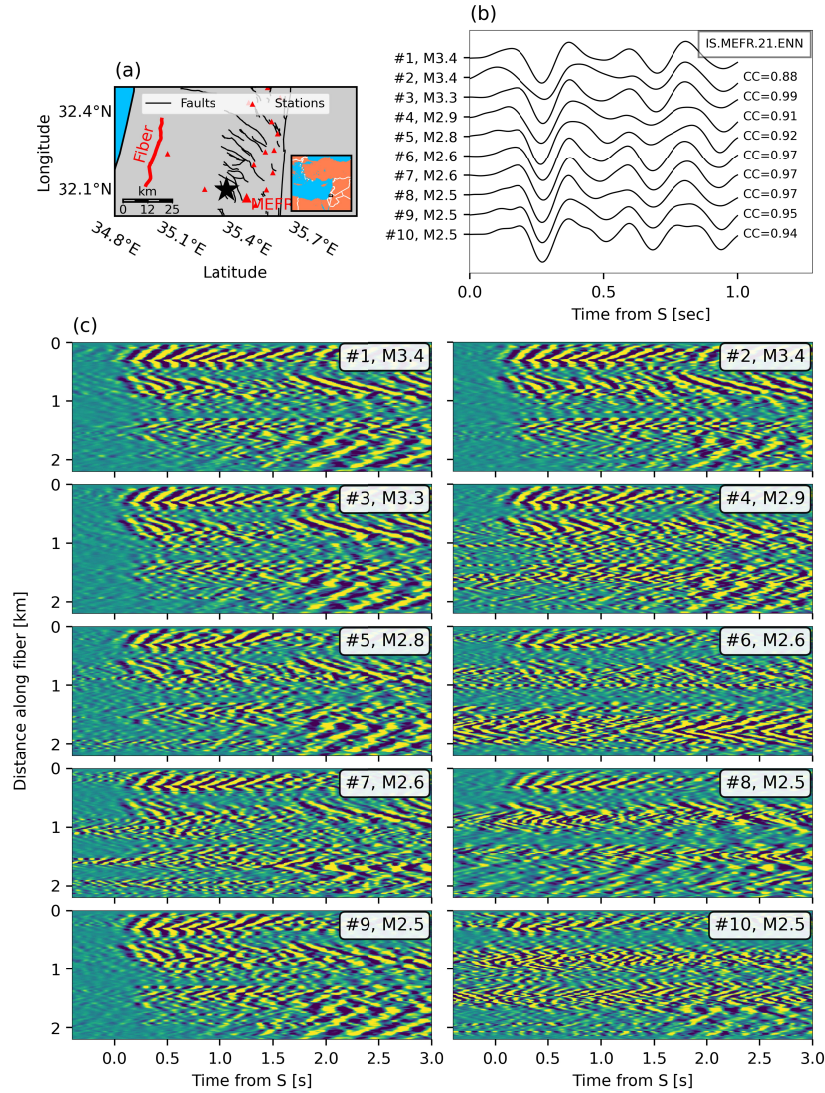


Figure 1. (a) Map of catalog earthquake location (black star), seismometer (red triangles), fiber (red curve) and known faults (black curves, from Sharon et al., 2020). The region is indicated by a black rectangle in the inset map. (b) The first second of the S-waves recorded by the north component of MEFR station are shown for all earthquakes. Waveforms are normalized and vertically shifted for visibility (catalog magnitudes indicated on the vertical axis; numbering as in Table S1). CC values for each waveform and the top one are indicated. (c) DAS strain-rate recordings of the first 3 seconds of the S-wave on a 2.2 km fiber segment for the different earthquakes. Each earthquake is normalized by its standard deviation. Earthquake numbering (corresponding to Table S1) and magnitudes are reported in each panel.

To obtain earthquake specific stacked Fourier spectra, few processing procedures were applied. First, theoretical arrival times from the earthquake source to all fiber channels were calculated and a move-out correction for the direct S-wave was applied. I use a uniform data interval of 20 seconds for all earthquakes, starting 1 second before the S-wave arrival. This data window is longer than the expected source durations of the analyzed earthquakes, and was chosen since it 1) produces reliable model fits (as described in the next section), 2) increases the

low frequency resolution that is useful to fit the lower frequency part of the spectra, and 3) yields a spatially averaged wavefield (Abercrombie, 2013; Baltay et al., 2010; Mayeda et al., 2007) that compensates for the single sensing direction (along the fiber) and the limited azimuthal observations of the earthquakes (fiber aperture of $\sim 45^\circ$). Move-out corrected strain-rates were then tapered using a 10% Tukey function and amplitude spectra were calculated and stacked by geometric averaging of channel-specific spectra.

Stacking amplitude spectra along the fiber has a pronounced smoothing effect. This behavior is visualized in Figure S1 for the M3.3 and M2.8 earthquakes, where seismometer spectra (panel a) and single DAS channel spectra (panel b) are compared to stacks of 1, 5, 19 km and the full fiber (panels c, d, e and f, respectively). When stacking over a longer spatial extent, local noises are suppressed and laterally coherent earthquake signals emerge, increasing the smoothness of the spectra. Furthermore, stacked spectra allow for clear separation between similar sized earthquakes which allows for reliable spectral ratio analysis, as further demonstrated.

The analysis is only reliable in a sufficiently high SNR frequency band that needs to be identified. Here, I used the same frequency band for all EGF pairs in order to reduce model fitting biases (Abercrombie, 2021). To determine the usable bandwidth, I calculated SNR using the spectra of the signal and pre-signal noise, both stacked over the entire fiber. The latter is calculated in an equivalent 20 second window. Stacked earthquake strain-rate amplitude spectra and stacked SNR (stacked signal divided by stacked noise) curves are plotted in Figure S2. To better determine the usable frequency band, SNR curves were resampled in equal log of frequency bins (e.g., Lior & Ziv, 2017) (panels b and d of Figure S2). Usually, EGF studies require an SNR threshold of at least 2 (e.g., Shearer et al., 2019; Viegas et al., 2010), however, when using stacked signals, this threshold can be relaxed, since stacked signal and noise spectra are smooth and exhibit less amplitude scatter, allowing for more precise differentiation of signal and noise. Thus, I only require that the stacked signals' spectral amplitudes are 10% above noise levels ($\text{SNR}=1.1$, horizontal black line in panels b and d of Figure S2). Even though this analysis facilitates a larger bandwidth, I set the usable bandwidth to be between 2 and 20 Hz. The validity of this frequency band will be later verified by inspecting model fits and parameter uncertainties. Two earthquakes did not meet the required SNR condition (#6 and #10) with low SNR between 10 and 20 Hz (Figure S2d), and an additional earthquake (#8) had unexpectedly high amplitudes at low frequencies (~ 0.5 to ~ 4 Hz) that deviate from the omega squared model in Equation (1) (dashed black curve in Figure S2a). In the following, the remaining 7 earthquakes are analyzed.

3 Spectral Ratios Application to DAS Data

Earthquake-specific stacked spectra were used to construct spectral ratios for different earthquake pairs. Model fitting and parameter uncertainty estimation is similar to that proposed by Viegas et al. (2010). The stacked spectra of the larger earthquakes are divided by those of the smaller ones. This procedure is mathematically equivalent to calculating the spectral ratios at every DAS channel, followed by stacking, because stacking is done via geometric averaging. The spectral ratios are then resampled in equal log-of-frequency bins and the logarithm of the spectral ratios are fitted with the logarithm of Equation (3) to obtain the best fitting $\log(M_{01}/M_{02})$, f_{01} and f_{02} estimates. The inversion was done using a non-linear least square approach, implemented via Python's SciPy `curve_fit` tool. Parameter uncertainties were estimated by varying the value of one parameter and calculating the standard deviation of the fit

while treating the other two parameters as free fitting coefficients. The parameter-specific uncertainty range is determined by a standard deviation increase of 5%.

The fits to the spectral ratios improve when the latter are stacked over longer fiber segments as demonstrated in Figure 2 and S3. In these examples, spectral ratios are obtained for magnitude 3.3 and 2.8 earthquakes using MEFR accelerometer (panel a), a single DAS channel (panel b), stacks of 1, 5 and 19 km (panels c, d and e, respectively), and the full fiber (panel f). Fits are quantified using the standard deviation and R^2 (panel legends), and corner frequency uncertainties (error bars). The fits in Figures 2 and S3 are obtained using the Boatwright ($\gamma = 2$ in Equation 3) and Brune ($\gamma = 1$ in Equation 3) models, respectively. The Boatwright model, with sharper corner frequencies, clearly outperforms the Brune model, producing better fits and lower parameter uncertainties. Thus, the Boatwright model is used in following analysis. While using a single accelerometer (panels a) produced slightly better fits than a single DAS channel (panels b), stacking over longer segments significantly reduces the scatter in the spectral ratios and dramatically improves the fits (panels c-f).

I calculate model fits to all EGF pairs using full fiber stacks, only considering pairs whose magnitudes differ by at least 0.4 units. The spectral ratios, fits and goodness of fit parameters are shown in Figure 3 for 12 earthquake pairs. Highly reliable fits are obtained, with consistent (within error bars) earthquake-specific corner frequencies among different EGF pairs.

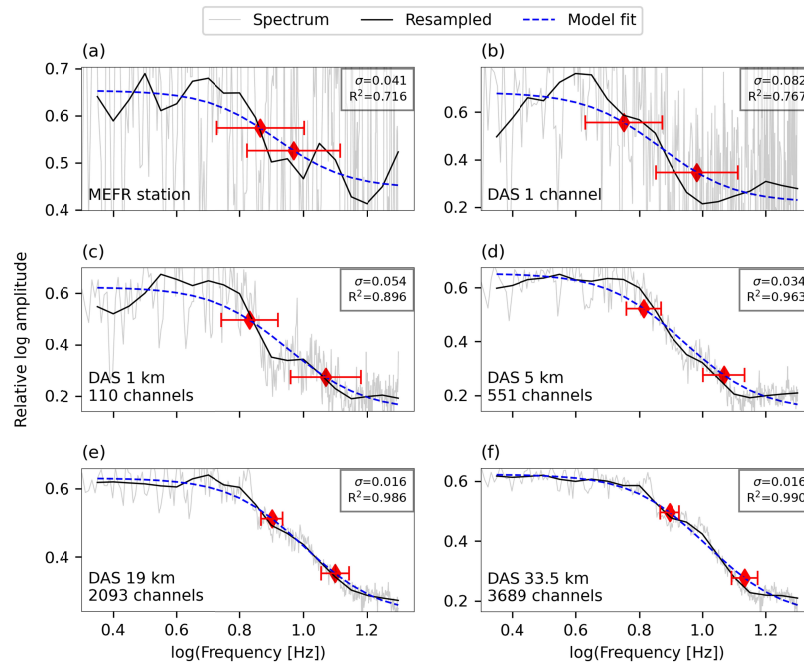


Figure 2. Spectral ratios and fits using the Boatwright ($\gamma = 2$ in Equation 3) model for magnitudes 3.3 and 2.8. Spectral ratios at (a) MEFR station (geometric mean of both horizontal components), (b) a single DAS channel, and stacks of (c) 1 km, (d) 5 km, (e) 19 km and (f) the full fiber. DAS stacks were centered around km 19 along the fiber. Spectral ratios or stacked ratios, resampled ratios, and model fits are indicated by thin grey curves, black curves, and blue curves, respectively. Standard deviations and R^2 are indicated in the panel legends, corner frequency uncertainties are indicated by red error bars.

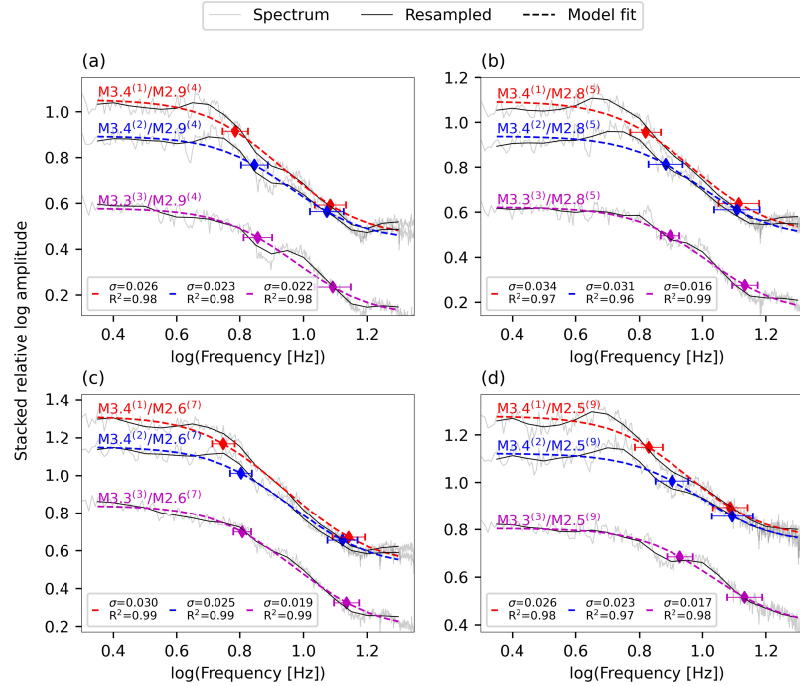


Figure 3. Spectral ratios fits using the Boatwright ($\gamma = 2$ in Equation 3) model for different earthquake pairs. Stacked spectral ratios, resampled ratios and model fits are indicated by thin grey curves, black curves, and colored curves, respectively. Standard deviations and R^2 are indicated in the panel legends, corner frequency uncertainties are indicated by horizontal error bars. Red, blue and purple curves correspond to different larger earthquake while each panel shows a specific smaller earthquake.

4 Implications for Source Parameter Studies

The spectral ratios method produces accurate corner frequencies, but only relative seismic moments; for accurate stress drops, reliable moment estimations are needed (Equation 2). The obtained results are unique in that each of the 7 earthquakes is used for 3 or 4 different EGF pairs (Figure 3), resulting in several corner frequency and relative moment estimates per earthquake, such that all moments may be estimated if one is known. Here, seismic moments were determined using a linear least-squares inversion, detailed in Text S2, where the magnitude of the largest earthquake was fixed to its catalog moment magnitude of 4.3 (Table S1). The inversion produced stable earthquake specific seismic moments (Figure S4). Stress drops were then estimated via Equation 2 using the earthquake-specific seismic moments, the different corner frequencies, $k = 0.21$ (Madariaga, 1976) and $C_s = 3.2$ km/s. Event averaged source parameters are listed in Table S1. Figure 4 plots corner frequencies (panel a) and stress drops (panel b) as functions of earthquake-specific seismic moments. Fit-specific corner frequencies and stress drops are indicated by grey circles while event averages are indicated by red circles.

Corner frequency and stress drop within-event variabilities are larger for the 3 largest earthquakes compared to the 4 smallest ones (Figure 4), possibly since the larger corner of the EGF pairs, associated with the smallest earthquakes, is typically sharper than the smaller corner, associated with the largest earthquakes (Figure 3). This may be an artifact of the limited bandwidth, although corner frequencies are well resolved, present small uncertainties and are

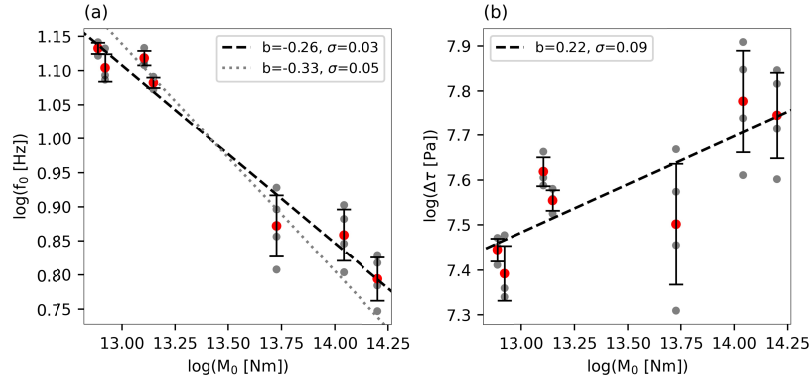


Figure 4. The logarithms of (a) corner frequencies and (b) stress drops as functions of the logarithm of seismic moments. Seismic moments were obtained using the least-squares inversion (Text S2) per earthquakes. Fit-specific and event averaged f_0 and $\Delta\tau$ are indicated by grey and red circles, respectively. Vertical error bars are the standard deviations to the different estimates. Linear fits to event averages are indicated by dashed black lines with slopes and standard deviations indicated in panel legends. The dotted curve in (a) is the fit assuming earthquake self-similarity (constant stress drop), i.e., a slope of $-1/3$.

sufficiently within the bandwidth limits (2 to 20 Hz). Alternatively, the observed scatter in the corner frequencies of the larger earthquakes may suggest complexities and variabilities among the noise conditions or source functions of the smaller earthquakes, that thus do not perform as ideal Green's functions.

Stress drop within-event variabilities are generally smaller than between-event variabilities (Figure 4b) demonstrating the robustness of these estimates and allowing for the analysis of stress drop variations with seismic moment. Stress drops span ~ 0.4 orders of magnitude while the available seismic moments span 1.3 orders of magnitude. In spite of the limited parameter ranges, it is clearly seen that the stress drops of the largest earthquakes are larger than those of the smaller ones by a difference of ~ 0.4 orders of magnitude (Figure 4 and Table S1). Linear fits to event averages in Figure 4 support this trend, indicating that $\log(\Delta\tau) \propto 0.22 \log(M_0)$. However, given the small number of observations and limited magnitude range, this scaling relation should be treated with caution and cannot be reliably extrapolated. Further investigations into the temporal evolution of the studied earthquakes considering both local (seismicity patterns near the Dead-Sea Transform) and regional (the relation to the 2023 Turkey earthquakes) effects is required to better interpret the obtained source parameters.

5 Conclusions

In this work, I demonstrated the robustness of DAS for source parameter estimation via the spectral ratios method applied to 7 repeating earthquakes in central Israel. Stacking move-out corrected amplitude spectra along the fiber significantly reduced the effect of incoherent and locally-coherent noises, producing a smoother and more coherent earthquake spectra. These stacked spectra allow for the application of the EGF method even for similar sized earthquakes. I calculated spectral ratios for different EGF pairs, and obtained excellent fits to the model with robust and stable estimates of seismic moment ratios and both corner frequencies. Fits obtained using the Boatwright model (Figure 2) significantly outperform those obtained using the Brune model (Figure S3). Having prior knowledge of one earthquake moment magnitude, I performed a linear least-squares inversion to obtain earthquake specific seismic moments and stress drop.

The obtained source parameters are very reliable, as indicated by the excellent spectral ratios model fits, allowing for in-depth investigations of source properties and stress drop scaling with seismic moment. For these earthquakes, Source parameter analysis revealed that stress drop increases with seismic moment. However, a more in-depth analysis of stress drop behavior considering the temporal evolution of the analyzed sequence is required.

The results demonstrate the great potential of DAS for earthquake source studies: 1) Owing to the abundance of DAS measurements, stacked along the fiber, SNR requirements were reduced to $\text{SNR} > 1.1$, allowing for less restrictive application of the EGF method. This property is especially beneficial for small earthquakes ($M < 3$) that typically suffer from low SNR and are reliably recorded by fewer stations. Furthermore, having additional possible earthquake pairs for the same dataset, improves the stability of source parameter inversion. 2) Spectral ratios stacked along the fiber exhibit excellent fits to the model and circumvent the need to stack over many seismic stations in a broad azimuthal range, potentially facilitating investigation of azimuthal source parameter variations. This property may also allow for better separation of source from path and site effects. 3) The EGF method applied to DAS circumvents the need to convert DAS measurements to ground motions for source parameter inversion (Lior et al., 2023; Lior, Sladen, Mercerat, et al., 2021). Finally, DAS can improve our knowledge of the relation between source parameters and ground motion variabilities, as well as our understanding of source complexities in various sized earthquakes.

Acknowledgments

The author thanks Prisma Photonics for their extensive help and support in data acquisition, handling and transfer.

Open Research

Seismometer data can be downloaded from the Geological Survey of Israel (<https://eq.gsi.gov.il/en/earthquake/searchEQS.php>), and data to reproduce the results is found at <https://osf.io/y8csp/>.

References

- Abercrombie, R. E. (2013). Comparison of direct and coda wave stress drop measurements for the Wells, Nevada, earthquake sequence: Comparison of Direct and Coda Wave Stress Drop Measurements. *Journal of Geophysical Research: Solid Earth*, 118(4), 1458–1470. <https://doi.org/10.1029/2012JB009638>
- Abercrombie, R. E. (2021). Resolution and uncertainties in estimates of earthquake stress drop and energy release. *Philosophical Transactions of the Royal Society A: Mathematical, Physical and Engineering Sciences*, 379(2196), 20200131. <https://doi.org/10.1098/rsta.2020.0131>

- Abercrombie, R. E., Bannister, S., Ristau, J., & Doser, D. (2017). Variability of earthquake stress drop in a subduction setting, the Hikurangi Margin, New Zealand. *Geophysical Journal International*, 208(1), 306–320. <https://doi.org/10.1093/gji/ggw393>
- Aki, K., & Richards, P. G. (2002). *Quantitative seismology* (2nd ed). University Science Books.
- Al-Ismail, F., Ellsworth, W. L., & Beroza, G. C. (2023). A Time-Domain Approach for Accurate Spectral Source Estimation with Application to Ridgecrest, California, Earthquakes. *Bulletin of the Seismological Society of America*, 113(3), 1091–1101. <https://doi.org/10.1785/0120220228>
- Baltay, A., Prieto, G., & Beroza, G. C. (2010). Radiated seismic energy from coda measurements and no scaling in apparent stress with seismic moment. *Journal of Geophysical Research: Solid Earth*, 115(B8). <https://doi.org/10.1029/2009JB006736>
- Boatwright, J. (1980). A spectral theory for circular seismic sources; simple estimates of source dimension, dynamic stress drop, and radiated seismic energy. *Bulletin of the Seismological Society of America*, 70(1), 1–27. <https://doi.org/10.1785/BSSA0700010001>
- Brune, J. N. (1970). Tectonic stress and the spectra of seismic shear waves from earthquakes. *Journal of Geophysical Research*, 75(26), 4997–5009. <https://doi.org/10.1029/JB075i026p04997>
- Chen, X. (2023). Source parameter analysis using distributed acoustic sensing – an example with the PoroTomo array. *Geophysical Journal International*, 233(3), 2207–2213. <https://doi.org/10.1093/gji/ggad061>

- 303 Eshelby, J. D. (1957). The determination of the elastic field of an ellipsoidal inclusion, and
304 related problems. *Proceedings of the Royal Society of London. Series A. Mathematical
305 and Physical Sciences*, 241(1226), 376–396. <https://doi.org/10.1098/rspa.1957.0133>
- 306 Huang, Y., Ellsworth, W. L., & Beroza, G. C. (2017). Stress drops of induced and tectonic
307 earthquakes in the central United States are indistinguishable. *Science Advances*, 3(8),
308 e1700772. <https://doi.org/10.1126/sciadv.1700772>
- 309 Ide, S., & Beroza, G. C. (2001). Does apparent stress vary with earthquake size? *Geophysical
310 Research Letters*, 28(17), 3349–3352. <https://doi.org/10.1029/2001GL013106>
- 311 Kaneko, Y., & Shearer, P. M. (2015). Variability of seismic source spectra, estimated stress
312 drop, and radiated energy, derived from cohesive-zone models of symmetrical and
313 asymmetrical circular and elliptical ruptures. *Journal of Geophysical Research: Solid
314 Earth*, 120(2), 1053–1079. <https://doi.org/10.1002/2014JB011642>
- 315 Kurzon, I., Nof, R. N., Laporte, M., Lutzky, H., Polozov, A., Zakosky, D., Shulman, H.,
316 Goldenberg, A., Tatham, B., & Hamiel, Y. (2020). The “TRUAA” Seismic Network:
317 Upgrading the Israel Seismic Network—Toward National Earthquake Early Warning
318 System. *Seismological Research Letters*, 91(6), 3236–3255.
319 <https://doi.org/10.1785/0220200169>
- 320 Lior, I., Rivet, D., Ampuero, J.-P., Sladen, A., Barrientos, S., Sánchez-Olavarria, R., Villarroel
321 Opazo, G. A., & Bustamante Prado, J. A. (2023). Magnitude estimation and ground
322 motion prediction to harness fiber optic distributed acoustic sensing for earthquake early
323 warning. *Scientific Reports*, 13(1), Article 1. <https://doi.org/10.1038/s41598-023-27444-3>
- 324 Lior, I., Sladen, A., Mercerat, D., Ampuero, J.-P., Rivet, D., & Sambolian, S. (2021). Strain to
325 ground motion conversion of distributed acoustic sensing data for earthquake magnitude

and stress drop determination. *Solid Earth*, 12(6), 1421–1442. <https://doi.org/10.5194/se-12-1421-2021>

Lior, I., Sladen, A., Rivet, D., Ampuero, J., Hello, Y., Becerril, C., Martins, H. F., Lamare, P., Jestin, C., Tsagkli, S., & Markou, C. (2021). On the Detection Capabilities of Underwater Distributed Acoustic Sensing. *Journal of Geophysical Research: Solid Earth*, 126(3). <https://doi.org/10.1029/2020JB020925>

Lior, I., & Ziv, A. (2017). The Relation between Ground Acceleration and Earthquake Source Parameters: Theory and Observations. *Bulletin of the Seismological Society of America*, 107(2), 1012–1018. <https://doi.org/10.1785/0120160251>

Lior, I., & Ziv, A. (2018). The Relation Between Ground Motion, Earthquake Source Parameters, and Attenuation: Implications for Source Parameter Inversion and Ground Motion Prediction Equations. *Journal of Geophysical Research: Solid Earth*, 123(7), 5886–5901. <https://doi.org/10.1029/2018JB015504>

Madariaga, R. (1976). Dynamics of an expanding circular fault. *Bulletin of the Seismological Society of America*, 66(3), 639–666.

Mateeva, A., Lopez, J., Potters, H., Mestayer, J., Cox, B., Kiyashchenko, D., Wills, P., Grandi, S., Hornman, K., Kuvshinov, B., Berlang, W., Yang, Z., & Detomo, R. (2014). Distributed acoustic sensing for reservoir monitoring with vertical seismic profiling: Distributed acoustic sensing (DAS) for reservoir monitoring with VSP. *Geophysical Prospecting*, 62(4), 679–692. <https://doi.org/10.1111/1365-2478.12116>

Mayeda, K., Malagnini, L., & Walter, W. R. (2007). A new spectral ratio method using narrow band coda envelopes: Evidence for non-self-similarity in the Hector Mine sequence. *Geophysical Research Letters*, 34(11). <https://doi.org/10.1029/2007GL030041>

- Papp, B., Donno, D., Martin, J. E., & Hartog, A. H. (2017). A study of the geophysical response of distributed fibre optic acoustic sensors through laboratory-scale experiments: Geophysical response of fibre optic sensors. *Geophysical Prospecting*, 65(5), 1186–1204. <https://doi.org/10.1111/1365-2478.12471>
- Sato, T., & Hirasawa, T. (1973). Body wave spectra from propagating shear cracks. *Journal of Physics of the Earth*, 21(4), 415–431. <https://doi.org/10.4294/jpe1952.21.415>
- Sharon, M., Sagy, A., Kurzon, I., Marco, S., & Rosenshaft, M. (2020). Assessment of seismic sources and capable faults through hierarchic tectonic criteria: Implications for seismic hazard in the Levant. *Natural Hazards and Earth System Sciences*, 20(1), 125–148. <https://doi.org/10.5194/nhess-20-125-2020>
- Shearer, P. M., Abercrombie, R. E., Trugman, D. T., & Wang, W. (2019). Comparing EGF Methods for Estimating Corner Frequency and Stress Drop From *P* Wave Spectra. *Journal of Geophysical Research: Solid Earth*, 124(4), 3966–3986. <https://doi.org/10.1029/2018JB016957>
- van den Ende, M. P. A., & Ampuero, J.-P. (2021). Evaluating seismic beamforming capabilities of distributed acoustic sensing arrays. *Solid Earth*, 12(4), 915–934. <https://doi.org/10.5194/se-12-915-2021>
- Viegas, G., Abercrombie, R. E., & Kim, W.-Y. (2010). The 2002 M5 Au Sable Forks, NY, earthquake sequence: Source scaling relationships and energy budget. *Journal of Geophysical Research: Solid Earth*, 115(B7). <https://doi.org/10.1029/2009JB006799>
- Wu, Q., Chen, X., & Abercrombie, R. E. (2019). Source Complexity of the 2015 Mw 4.0 Guthrie, Oklahoma Earthquake. *Geophysical Research Letters*, 46(9), 4674–4684. <https://doi.org/10.1029/2019GL082690>